Capacitive Electronic Metal–Support Interactions: Outer Surface Charging of Supported Catalyst Particles

Tobias Binninger,[1,*] Thomas J. Schmidt,[1,2] and Denis Kramer[3,†]

[1] *Paul Scherrer Institut, Electrochemistry Laboratory, CH-5232 Villigen PSI, Switzerland*

[2] *ETH Zürich, Laboratory of Physical Chemistry, CH-8093 Zürich, Switzerland*

[3] *University of Southampton, Engineering Sciences, SO17 1BJ Southampton, United Kingdom*

Abstract

Electronic metal–support interactions (EMSI) in catalysis are commonly rationalized in terms of an electron transfer between support material and supported metal catalyst particles. This general perspective, however, cannot fully explain experimentally observed EMSI for metallic nanoparticulate catalysts, because the strong charge screening of metals should locally confine effects of direct electronic interaction with the support to the catalyst–support interface (CSI), which, apart from the perimeter, is largely inaccessible for catalysis reactants. The concept of capacitive EMSI is proposed here for catalyst particles at the nanometer scale, where electronic equilibration results in a long-range charging of the catalytically active outer surface (CAOS) bypassing the expected strong metallic charge screening, which is confirmed and quantified by electrostatic and density functional theory simulations revealing a strong dependence on the coverage of the support surface with catalyst particles. This long-range charge transfer leads to a shift of the local work function at the CAOS. In order to describe the catalytic consequences, an amendment of d-band theory in terms of 'd-band + work function' is proposed. Furthermore, the charging of remote catalytic sites at the CAOS scales with the relative dielectric constant of the surrounding medium and it is concluded that EMSI can have surprisingly strong influence especially in the presence of a strongly polarisable dielectric.

Keywords: electronic metal–support interactions, supported catalyst nanoparticles, charge transfer, particle surface charging, dielectric media, work function, d-band theory, heterogeneous catalysis, electrocatalysis

I. INTRODUCTION

Nanoscopic metal catalyst particles supported on metal oxides or carbon materials constitute the majority of heterogeneous catalysts and electrocatalysts used in the chemical industry and studied in catalysis research[1,2]. Furthermore, urgently needed solutions for major global challenges, like global warming and a growing energy demand, will depend on the availability of efficient catalysts.

It was early recognized that the support material can influence the catalytic activity of metal catalyst particles[3]. Besides explanatory schemes based, e.g., on structural or compositional modifications, this 'carrier effect' has been explained by an electron transfer between support material and metal catalyst particles[4,5]. Such 'electronic metal–support interactions' (EMSI)[6] can be rationalized in terms of an electron transfer for metal adatoms and small sub-nanometer sized metal clusters[7–11] due to the formation of polar chemical bonds with more or less ionic character between the support surface atoms and the metal cluster 'adsorbate'. Substantial charge transfer of the order of 0.1–1 |e|/atom can be observed when metal adatoms or sub-nm clusters interact directly with the support surface[12], especially with oxide support defects or with surface cations of transition metal oxides[11]. This strong electron transfer corresponds to a partial oxidation or reduction of the supported metal atoms with drastic influence on their catalytic properties.

For metallic nanoparticles, a different classification of EMSI emerges: the large number of electronic degrees of freedom of nanometer sized metal particles leads to the formation of a continuum of electronic states with a well-defined Fermi level[13] and an associated work function of the metal nanoparticle. As a consequence, a thermodynamic description of EMSI is justified, where electron transfer is rationalized in terms of electronic equilibration between the support material and the catalyst nanoparticle in analogy to the Schottky theory of metal/semiconductor contacts[3,4,14,15]. At the sub-nanometer scale, the majority of metal cluster atoms are in direct contact with the support surface, especially in the case of monolayer thick two-dimensional clusters. For nanoparticles, where the majority of surface atoms is not in direct contact with the support, the question arises whether EMSI can affect sites at the catalytically active outer surface (CAOS) in addition to how the amount of EMSI-related electron transfer scales with particle size[16]. Due to strong charge screening[17], the excess charge on metal nanoparticles could be expected to accumulate at the

direct contact interface between the metal particle and the support material (the catalyst–support interface, CSI), thus forming a charged double layer at the CSI. In line with this expectation, computational studies on transition metal overlayers fully covering carbon[18] or metal oxide[19] support surfaces came to the conclusion that electronic interactions between metal and support only affect the first two to three metal overlayers. However, as shown in the following, basic electrostatic considerations suggest that, in addition to the sub-nm short-range charge transfer at the CSI, electronic equilibration with the support material leads to a long-range direct charging of the catalyst nanoparticle CAOS, which can affect remote catalytic sites at a distance up to several nanometers away from the CSI.

II. RESULTS

A. Theoretical derivation of catalyst particle outer surface charging

Figure 1 illustrates the electrostatic argument. In general, the isolated catalyst particles will have a work function W_{c} distinct from the work function W_{s} of the bare support surface (cf. Figure 1a). Upon contact, the support material equilibrates with each of the catalyst particles by electron transfer. The resulting polarization generates an electrostatic potential energy step $(-e)\Delta\Phi_{\mathrm{s-c}}$ across the CSI that equilibrates the Fermi levels and is equal to the difference of the two work functions $W_{\mathrm{c}} - W_{\mathrm{s}}$ (cf. Figure 1b). The corresponding polarization double-layer is localized at the CSI due to the strong charge screening inside the metal catalyst particles. This basic reasoning of charge transfer at the direct CSI is well-understood[15,20].

An additional long-range charging of the CAOS of the catalyst particles must occur if the catalyst particles do not fully cover the support surface. The overlapping dipole fields of each of the supported, polarized catalyst particles generate an overall electrostatic potential step between support and vaccum (dielectric) $\Delta\Phi_{\mathrm{s-v}}$ (cf. Figure 1c) that is proportional to the average surface polarization density $\langle p \rangle$ (cf. proof in the Appendix),

$$\Delta\Phi_{\mathrm{s-v}} = \langle p \rangle / (\epsilon_0 \epsilon_r) \ , \tag{1}$$

with the vacuum dielectric constant ϵ_0 and, in case the surface is surrounded by a dielectric medium instead of vacuum, the corresponding relative dielectric constant ϵ_r. Because the average surface polarization density $\langle p \rangle$ is a function of the support surface coverage with

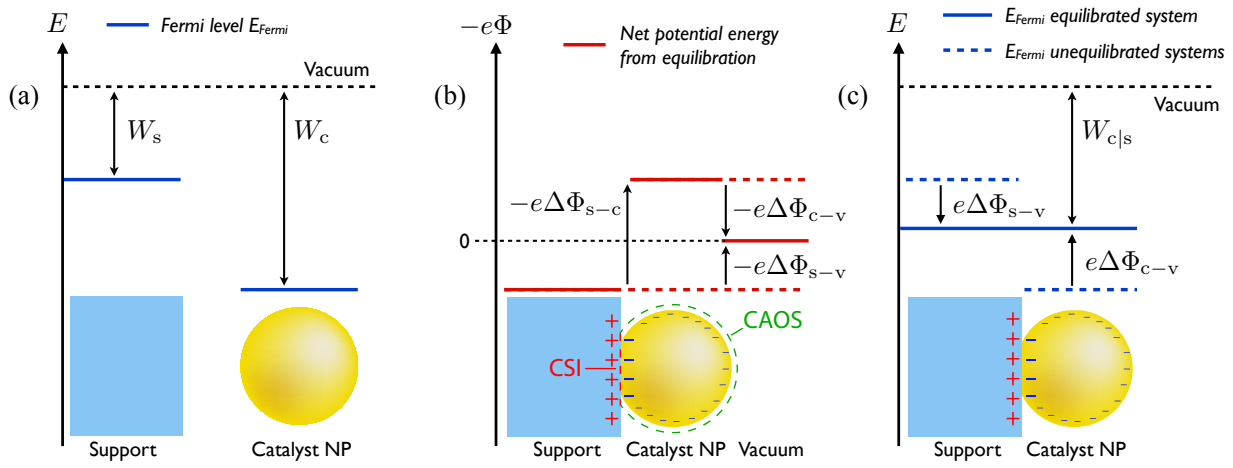

Figure 1. Schematic of energy levels, work functions, and electrostatic potentials. a) Work functions of the isolated support and catalyst particles; b) illustration of the additional net electrostatic energy contribution $(-e)\Phi$ resulting from electronic equilibration. The zero potential level is chosen to correspond to the potential level in vacuum. An outer surface charge on the catalyst particle is necessary to account for the difference $\Delta\Phi_{c-v}$ of the net electrostatic potential levels in vacuum and inside the catalyst particle, respectively; c) the equilibrated system is characterized by a common Fermi level and work function $W_{c|s}$.

catalyst particles, the same holds for $\Delta\Phi_{s-v}$. Therefore, the overall surface potential step $\Delta\Phi_{s-v}$ is generally smaller in magnitude than $\Delta\Phi_{s-c}$ at the direct CSI, which is fixed by $W_c - W_s$, for an incomplete coverage of the support surface with catalyst particles. This difference between $\Delta\Phi_{s-v}$ and $\Delta\Phi_{s-c}$ is compensated by an additional charge on the CAOS of each catalyst particle. The electrostatic field associated with this additional CAOS charge generates the required additional electrostatic potential step $\Delta\Phi_{c-v}$ in order to ensure that the value of the electrostatic potential in vacuum is path-independent (cf. Figure 1b):

$$\Delta\Phi_{s-v} = \Delta\Phi_{s-c} + \Delta\Phi_{c-v} \ . \tag{2}$$

Furthermore, the additional surface charge on the CAOS of the catalyst particle generates a field contribution inside the particle which opposes the dipole field originating from the polarized CSI, thus fulfilling the requirement of zero net electrostatic field inside the bulk of the metal catalyst particle, which has been pointed out earlier in the context of a Schottky model for metal nanoparticles on semiconductor surfaces[15,21,22].

B. Electrostatic model simulations

The magnitude of the CAOS charging effect can be estimated with a classical electrostatic model. Simulations were performed with COMSOL. The support material and the catalyst particles were modelled without loss of generality as perfect conductors with a fixed electrostatic potential difference of 1 V between catalyst particle and support, corresponding to a work function difference of 1 eV. A catalyst particle was placed above the support surface inside a cuboid supercell with edge length $l_{\text{c-c}}$ and periodic boundary conditions in x- and y-direction parallel to the surface. The system is equivalent to a 2-dimensional square array of catalyst particles with inter-particle distance $l_{\text{c-c}}$. Different geometries of the catalyst particle were used: hemispherical, spherical, and cubical. The distance between the support surface and the flat bottom particle surface was fixed at $d_{\text{c-s}} = 0.3\,\text{nm}$. The numerical convergence of the electrostatic simulations was confirmed by refinement of the 3-dimensional finite element mesh. In order to calculate the net electrostatic potential Φ and the surface charge density σ generated by the electronic equilibration between the support material and the catalyst particle, the support surface was grounded ($\Phi_{\text{s}} = 0\,\text{V}$) and the catalyst particle potential $\Phi_{\text{c}} = 1\,\text{V}$ was fixed for a hypothetical work function difference of $W_{\text{c}} - W_{\text{s}} = -1\,\text{eV}$. Due to the linearity of Poisson's equation, the results for any other work function difference can be obtained by linear scaling.

Figure 2 plots the electrostatic potential Φ and the surface charge density σ on the support surface and the CAOS for hemispherical catalyst particles. It becomes obvious that not only the entire CAOS of the particle carries charge, but also the surrounding empty support surface. The CAOS charge density gradually decreases towards the top of the catalyst particle. However, even the minimum value of $\sigma_{\text{c}}(\theta = 0) = 0.049\,e/\text{nm}^2$ is substantial (cf. $\sigma_{\text{c}} = 0.184\,e/\text{nm}^2$ at the direct CSI), leading to strong electrostatic fields of the order of $|E| \approx 1\,\text{V/nm}$ at the CAOS with increasing strength towards the perimeter of catalyst particle and support.

The same model can be used to gauge the dependence of the CAOS charging effect on catalyst loading and particle geometry. Figure 3 shows the surface polarization density per catalyst particle $\langle p \rangle_{A_{\text{c}}}$, averaged over the projected particle area A_{c}, as a function of the support surface coverage with particles $\gamma = A_{\text{c}}/A_{\text{total}}$. Catalyst particle polarization, and thus particle CAOS charging, is largest in the limit of low coverage γ. For increasing cover-

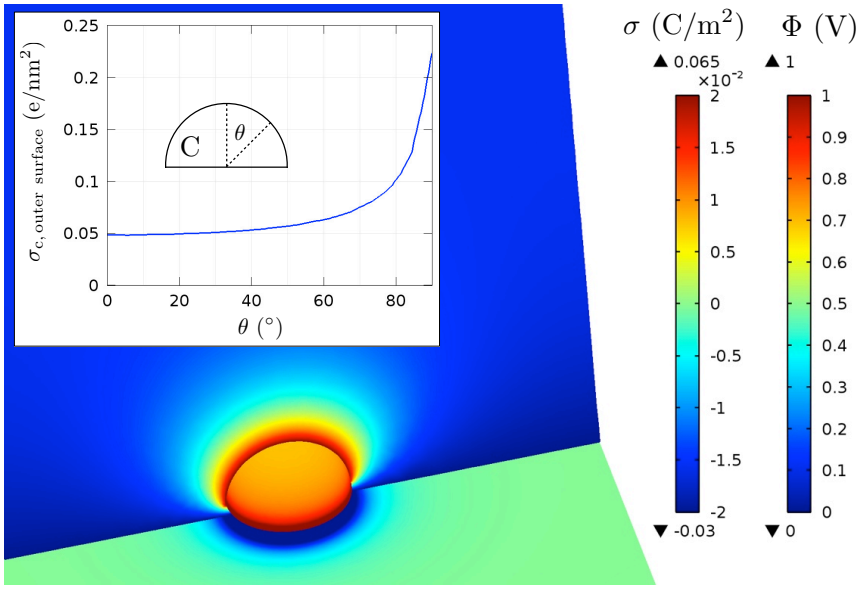

Figure 2. Electrostatic model results. Surface charge density σ on the outer catalyst surface and the support surface and the electrostatic potential Φ for a hemispherical catalyst particle with a diameter of 3 nm. Inset: Angular dependence of the outer catalyst surface charge density.

age, the CAOS charging decreases. This depolarization results from the mutual interaction between neighboring polarized particles. In the limit of large coverage $\gamma \to 1$, the CAOS charging converges to zero and $\langle p \rangle_{A_c}$ converges towards the fixed polarization p_0 at the direct CSI for a dense catalyst metal layer. Furthermore, the CAOS charging is very sensitive to the particle shape at small γ: the polarization density for $\gamma \to 0$ of hemispherical catalyst particles is less than half that of spherical and cubical particles.

C. Density functional theory simulations

Predictions of the classical electrostatic model were further investigated by density functional theory (DFT). Platinum nanoparticles supported on a Sb-doped SnO_2 (110) surface were chosen for this purpose, because this system has attracted substantial attention in recent research on electrocatalysts for the oxygen reduction reaction[23,24]. Periodic DFT computations were performed using the *Vienna Ab Initio Simulation Package* (VASP). The core electrons were taken into account by the projector augmented wave method (PAW)[25,26]. The generalized gradient approximation (GGA) in the PBE form[27] was used for the exchange-

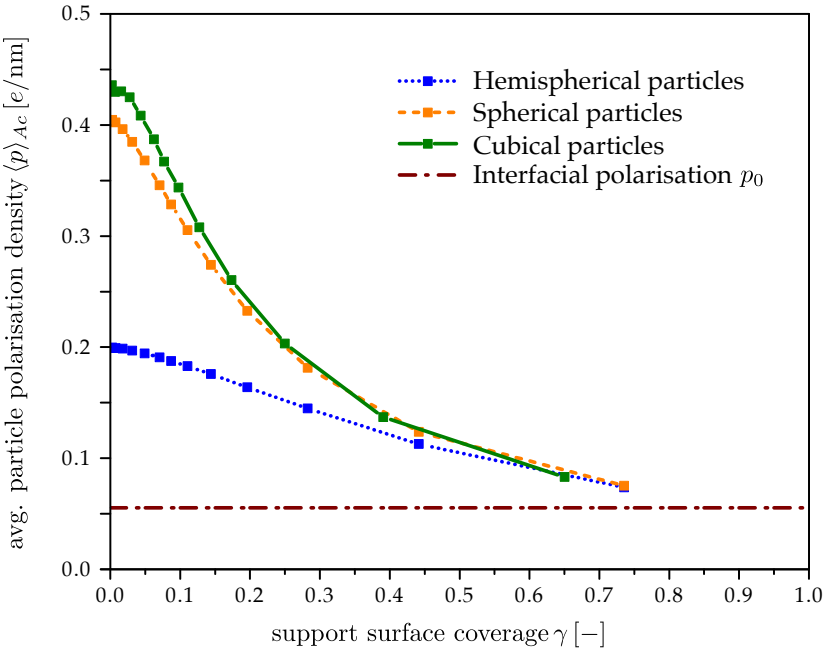

Figure 3. Electrostatic model results. Average surface polarization density per catalyst particle as a function of the support surface coverage with catalyst particles γ for different catalyst particle geometries.

correlation functional. The simulated system consisted of cuboctahedral Pt_{55} clusters supported on Sb-doped SnO_2 slabs comprising nine atomic layers with the most stable (110) surface orientation of the rutile crystal structure. Two different sizes of the periodic supercell were used in order achieve one system at high (1×1 supercell) and one at low coverage (2×2 supercell) with Pt nanoparticles. Stoichiometric and reduced Sb-SnO_2 (110) surfaces were used to introduce variations of the support work function. In order to extract purely electronic interactions, structural interactions between catalyst and support were excluded by fixing the geometries of the cuboctahedral Pt particles and the Sb-SnO_2 slab to those of the individual systems. A similar strategy has been applied in a DFT study of electronic Pt particle size effects[13]. Only the distance between the Pt cluster and the Sb-SnO_2 (110) surface was relaxed until an energy minimum was reached. Further details of DFT computations are described in the Appendix.

Figure 4 plots the net electrostatic potential energy $(-e)\Phi$ due to electronic equilibration across the surface for the three different systems. Figure 4a visualises 2D slices through

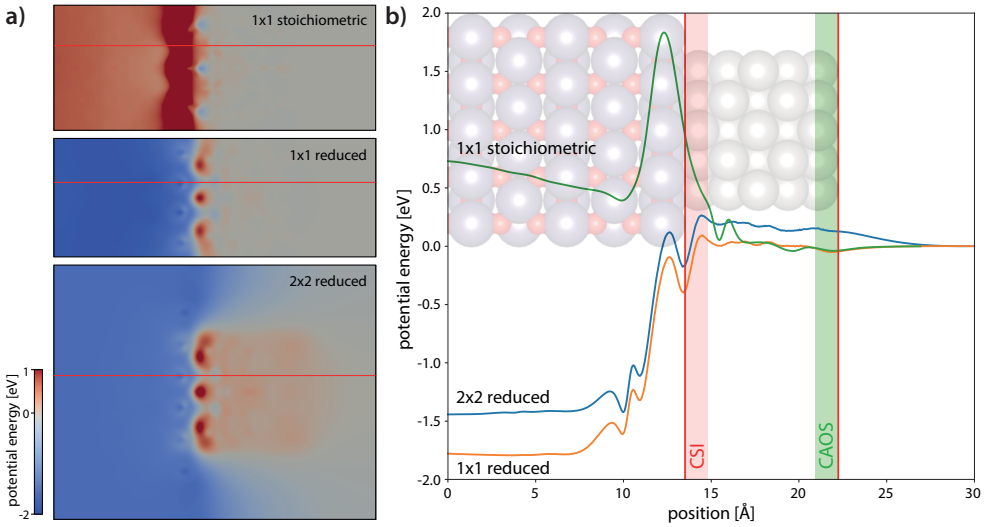

Figure 4. DFT results. (a) Color plots of the net electrostatic potential energy $(-e)\Phi$. (b) Plots of the net electrostatic potential energy $(-e)\Phi$ along a path Support–CSI–Pt particle–CAOS–Vacuum. The corresponding paths are indicated by horizontal lines in (a). Positions of different interfaces are indicated by vertical lines and visualized by a schematic drawing of the model.

the center of the particle, while Figure 4b compares line profiles along a path close to the particle centre as indicated by the red horizontal lines in the 2D plots. The net potential energy steps $(-e)\Delta\Phi_{\mathrm{s-c}}$ across the direct CSI are in good agreement with the work function differences $W_{\mathrm{c}} - W_{\mathrm{s}}$ between the individual systems of Pt particles and Sb-SnO_2 supports, cf. Table I for numerical values, which is opposite in sign for the stoichiometric support surface compared to the reduced surface. As predicted by the classical model, an additional potential gradient is present between the CAOS and vacuum for the low coverage system (2x2 supercell). This gradient corresponds to an electrostatic field strength of approx. 0.3 V/nm at the top surface, leading to a potential step of $(-e)\Delta\Phi_{\mathrm{c-v}} = 0.15\,\mathrm{eV}$ between Pt particle and vacuum. Towards the edge of the top surface, the electrostatic field strength reaches values exceeding 1.0 V/nm, cf. Figure 5c.

Figure 5b plots the net electron density change for the Pt/reduced Sb-SnO_2 system with 2x2 supercell. The Pt particle CAOS charging is clearly visible in terms of a halo around the CAOS corresponding to an increased electron density in agreement with the direction of electron transfer expected from the work function difference $W_{\mathrm{c}} - W_{\mathrm{s}}$. The change of electron number δ for each individual Pt atom of the nanoparticle as a result of electronic

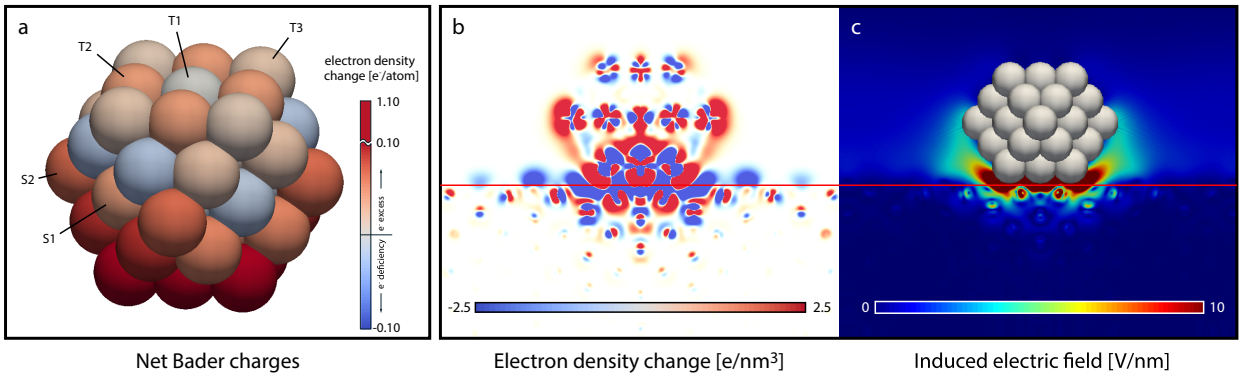

Figure 5. DFT results for the Pt/reduced Sb-SnO_2 system with 2x2 supercell. (a) Cuboctahedral Pt_{55} particle with color coding of transferred Bader charges per Pt atom. Positive values correspond to an increased electron number. The interface with the Sb-SnO_2 support is at the bottom. Also given is the Pt atom numbering referring to Table I. (b) Color plot of the net electron density change. (c) Color plot of the net electrostatic field strength in the vacuum space around the Pt particle CAOS. The position of the CSI is indicated by a horizontal line.

equilibration with the Sb-SnO_2 support was evaluated by Bader charge analysis[28]. Color coded values of δ are presented in Figure 5a; tabulated data can be found in Table I, averaged over different parts of the Pt particle as well as for specific Pt atoms labelled according to Figure 5a. In line with the sign of $W_c - W_s$, electrons are transferred on average to the Pt particle on the reduced Sb-SnO_2 surface, whereas electrons are withdrawn from the Pt particle on the stoichiometric support.

The average value of δ across the entire particle depends only weakly on supercell size and is with approximately $0.15\,e^-$/atom in good agreement with the order of magnitude of experimentally observed particle-averaged values reported for different systems in the literature[16,29]. However, the average without CSI is significantly smaller and drops to 0.016–$0.028\,e^-$/atom. Vice versa, an extremely large transfer of approximately $0.8\,e^-$/atom is found by taking the average only over the CSI. The average value over the entire Pt particle is, therefore, dominated by the electron transfer at the direct CSI, in agreement with experimentally observed increasing EMSI with increasing CSI contact area[30].

The coverage-dependent charging of the CAOS is weaker than charging at the CSI. Taking the average of δ only over the outer (100) facet of the Pt particle pointing towards vacuum results in a value of 0.023 electrons per Pt atom for the 2×2 supercell, which is in good

Table I. DFT results. Work function difference $W_c - W_s$ between the individual systems; Net potential energy step $(-e)\Delta\Phi_{s-c}$ across the direct CSI; Number of electrons transferred per Pt atom: Average (AVG) over the total Pt cluster, AVG without the first Pt layer in direct contact with the support (w/o CSI), AVG only over the first Pt layer in direct contact with the support (CSI), AVG only over the outer (100) facet towards vacuum; Specific Pt atoms: Atom C (cluster center), Atom S1 (side (100) facet center), Atom S2 (side corner), Atom T1 (outer (100) facet center), Atom T2 (outer edge), Atom T3 (outer corner), cf. Figure 5a. Values in e^-/atom with positive values corresponding to an increased electron number.

System	$W_c - W_s$	$(-e)\Delta\Phi_{s-c}$	AVG	AVG	AVG	AVG	Atom	Atom	Atom	Atom	Atom	Atom
$Pt/Sb\text{-}SnO_2$	[eV]	[eV]	total	w/o CSI	CSI	outer	C	S1	S2	T1	T2	T3
reduced, 2x2	+1.78[a]	+1.59	0.159	0.028	0.834	0.023	-0.015	0.041	0.066	-0.004	0.041	0.014
reduced, 1x1	+1.78	+1.77	0.145	0.016	0.804	0.001	0.007	-0.006	0.019	-0.003	-0.001	0.007
stoichio., 1x1	-0.76	-0.74	-0.006	-0.002	-0.028	0.000	-0.002	-0.016	-0.005	-0.002	0.004	-0.005

[a] The same value is given as for the 1x1 system. W_s is independent of the supercell size for periodic boundary conditions. The work function W_c of free Pt particles could have a slight dependence on the supercell size due to the different distances between the periodic images of the particles. This dependence, however, is expected to be small.

agreement with the order of magnitude of CAOS charging estimated from the classical electrostatic model assuming a metal surface atom density of approximately 12–15 atoms/nm^2. The average δ over the CAOS drops to almost zero for the 1×1 supercell confirming the strong dependence of CAOS charging on the coverage γ.

It can be concluded that quantitative analysis of electron transfer in terms of an average value over the entire catalyst particle[4,14,16,31] must be seen in a context of inhomogeneous charging across nanoparticles with strong localisation near the CSI, coverage dependend charging of the CAOS, and different weighting of CSI and CAOS depending on particle size and shape.

Finally, the analysis of individual Pt atoms furthermore confirms that the transferred charge accumulates at the surface of the Pt particle. The center atom is largely screened and the remaining net Bader charges of this atom, which appear uncorrelated with the

equilibration-driven charge transfer, both in magnitude and in sign, can be explained with Friedel oscillations[17] not being fully damped at the center atom for the 1 nm sized Pt particle. The effect of the long-range CAOS charging that circumvents the charge screening of the Pt particle bulk leads to a significant charge especially on edge Pt sites of the vacuum-facing facet, such as Pt atom T2, to which an amount of 0.041 electrons is transferred for the Pt/reduced Sb-SnO_2 system with 2×2 supercell. This transfer decreases to almost zero for the same system with 1×1 supercell and close proximity of neighboring Pt particles, a result that could indicate a close relationship with experimentally established catalyst particle proximity effects[32].

III. DISCUSSION

The long-range effect of EMSI at the nanometer scale can be described in terms of *catalysis in a capacitor*: The CAOS of the catalyst particle and the surrounding empty support surface correspond to the two charged electrodes of a capacitor at a voltage equal to the "built-in" potential difference $\Delta\Phi_{\mathrm{s-c}}$ between catalyst and support, which is fixed by the corresponding work function difference $W_{\mathrm{c}} - W_{\mathrm{s}}$. The influence of such "capacitive EMSI" on the properties of catalytic sites at the CAOS could be classified in terms of *electric field effects* and *surface potential effects* on the one hand, and direct *charge effects* due to the change of electron number at specific CAOS sites on the other hand, as discussed in the following.

According to Sabatier's principle, which is widely accepted in heterogeneous and in electro-catalysis, the binding energies of adsorbing species have a strong influence on the catalytic activity[33,34]. Prominent examples are the electrochemical reduction of oxygen on transition metal surfaces[35], which is governed by the respective oxygen adsorption energies, and the gas-phase synthesis of ammonia in the Haber-Bosch process, which can be correlated with the respective nitrogen adsorption energies[34].

a. Electric field effects of capacitive EMSI. The binding energies of adsorbates with polar bonds are influenced by the dipole–field interaction energy $E = -\mathbf{d} \cdot \mathbf{E}$ between the bond dipole $\mathbf{d}$ and the electrostatic field $\mathbf{E}$ at the CAOS. Typical dipole moments associated with polar adsorbate bonds are of the order of $0.01\,|\mathrm{e}|\mathrm{nm}$[36] yielding maximum changes of adsorbate binding energies of the order of 0.01 eV for field strengths of approx. $1\,\mathrm{V/nm}$ at the CAOS. Thus, electric field effects of capacitive EMSI via dipole–field interactions appear

to be comparably small.

b. Surface potential/work function effects of capacitive EMSI. Stronger catalytic effects due to capacitive EMSI can be expected from changes of the local work function[37], i.e. the surface potential at the CAOS[38], which arise from the strong electrostatic fields at the charged CAOS. Since the local work function influences the relative alignment of electronic adsorbate states and metallic surface states, strong implications for the catalytic properties can be expected[37,39]. These implications are discussed in more detail in the following proposing an amendment of *d*-band theory to include effects of the work function.

According to *d*-band theory, molecular adsorption energies are correlated with the position of the electronic *d*-band center ϵ_d with respect to the Fermi level ϵ_f of transition metal catalysts, because the relative positions of catalyst *d*-states, catalyst Fermi level ϵ_f, and HOMO/LUMO states E_i of the adsorbing molecule determine the strength of the splitting between bonding and anti-bonding adsorbate states and the degree of filling of the latter[40–42].

However, Figure 6 illustrates that the relative alignment of the interacting electronic states is determined not only by the position of the *d*-band center relative to the Fermi level of the transition metal, $\epsilon_f - \epsilon_d$, but also by the position of the Fermi level relative to the vacuum level, i.e. the work function W. In case that the adsorbate state is located entirely outside the surface potential step, it is the sum of work function and *d*-band center (relative to ϵ_f) that determines the energetic position of the metal *d*-states relative to the original molecular orbitals. Changes in the work function shift the metal *d*-states relative to the molecular states thereby altering the energetic resonance between these interacting states. This has a threefold effect on the binding energy of the adsorbate by changing (i) the absolute positions of bonding/anti-bonding adsorbate states with respect to the unperturbed states, (ii) the splitting between bonding and anti-bonding adsorbate states, and (iii) the degree of filling of anti-bonding adsorbate states.

This reasoning led us to revisit previously established correlations between catalytic activities and metal *d*-band centers. Figure 7 plots oxygen and nitrogen adsorption energies, as proxies of catalytic activity towards oxygen reduction and ammonia synthesis, as a function of *d*-band center (relative to ϵ_f) alone and *d*-band center plus work function, respectively (using values from Refs.[34,42–44]). In both cases, a stronger correlation is achieved if the work function is included in the consideration.

The extent to which the catalyst particle outer surface charging influences adsorbate

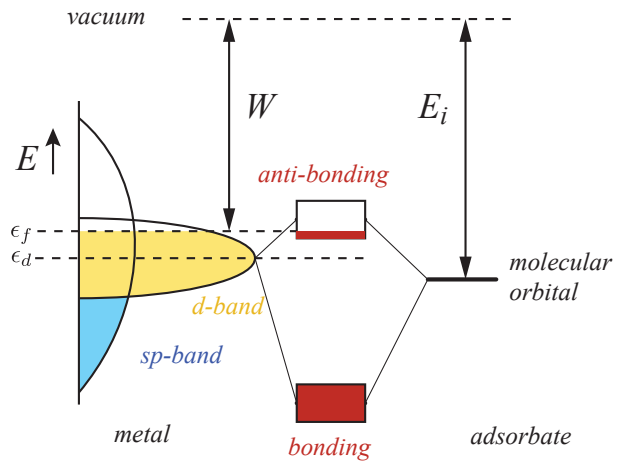

Figure 6. Illustration of the relevance of the work function in d-band theory for the relative alignment of energy levels and filling of anti-bonding states.

binding energies via changing the local work function depends critically on the distance at which the local work function is probed by the adsorbate. In photoemission of adsorbed xenon (PAX)[37], for instance, the surface potential is probed by electrons from an adsorbed Xe atom at a distance $d \approx 0.35\,\mathrm{nm}$ from the surface. The corresponding shift of the local work function due to capacitive EMSI can be estimated by the magnitude of the EMSI-induced electrostatic field $|E|$ directly at the surface, i.e. the gradient of the net electrostatic potential. As an example, for a value of $|E| \approx 1\,\mathrm{V/nm}$ as obtained from DFT, a shift of the local work function of the order of $0.35\,\mathrm{eV}$ can be expected.

Whereas the local work function can vary across different catalytic sites, the overall surface potential effect of capacitive EMSI can be quantified by the global work function $W_{\mathrm{c|s}}$ of the catalyst particle decorated support surface, cf. Appendix for a careful definition. The catalyst work function W_{c} is modified by the additional potential step $(-e)\Delta\Phi_{\mathrm{c-v}}$ between Pt particle and vacuum due to CAOS charging, so that the global work function equals

$$W_{\mathrm{c|s}} = W_{\mathrm{c}} - e\Delta\Phi_{\mathrm{c-v}} \ . \tag{3}$$

Figure 8 plots $W_{\mathrm{c|s}}$ as a function of the support surface coverage with catalyst particles γ obtained from electrostatic model simulations. At low coverage $\gamma \to 0$, the global work function strongly deviates from W_{c} and converges towards that of the bare support sur-

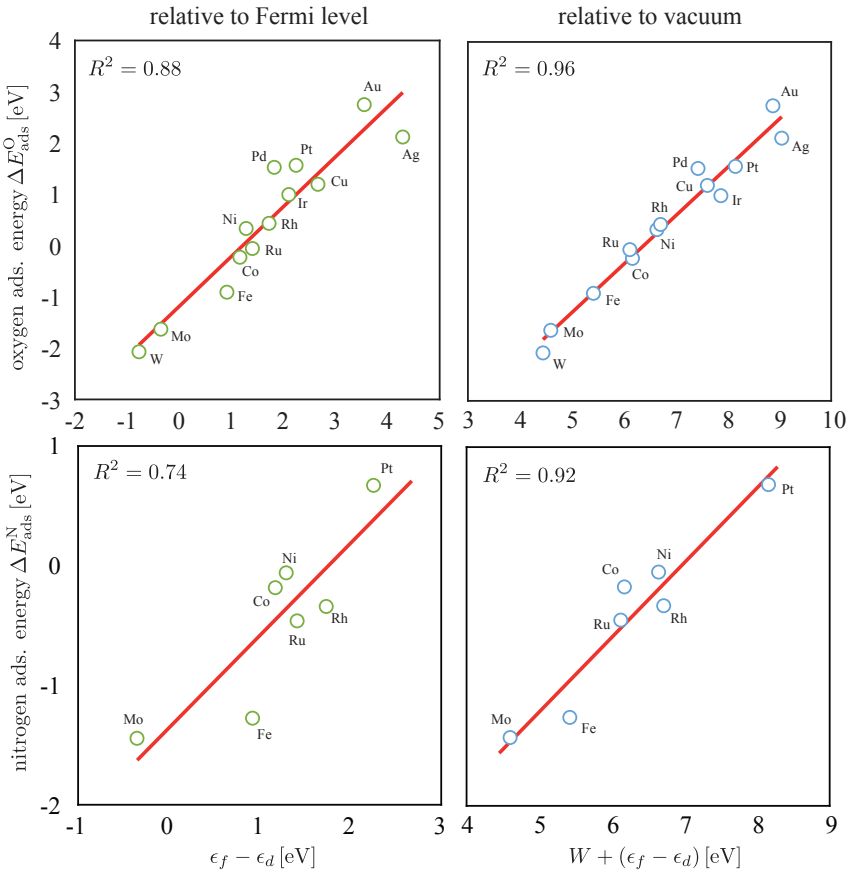

Figure 7. Correlation of oxygen (top) and nitrogen (bottom) binding energies on transition metal surfaces with transition metal *d*-band center relative to the Fermi level, $\epsilon_f - \epsilon_d$, (left) and relative to vacuum, $W + (\epsilon_f - \epsilon_d)$, (right). Data taken from Refs.[34,42–44].

face. Thus, capacitive EMSI can significantly change the work function at the CAOS with consequences for adsorbate binding energies as discussed above.

c. Charge and Dielectric effects of capacitive EMSI. Based on DFT results, a long-range CAOS electron transfer of up to 0.04 |e|/atom can be expected. It appears unclear, whether such moderate modifications in electron numbers can significantly influence adsorbate binding energies, e.g. via changes in the filling of adsorbate related (anti-)bonding orbitals. However, in analogy to the effect of a dielectric inside a capacitor, CAOS charging is expected to scale with the relative dielectric constant of the medium that surrounds the catalyst nanoparticle-decorated support surface. As discussed above, the CAOS of the catalyst particle and the surrounding empty support surface can be regarded as two charged

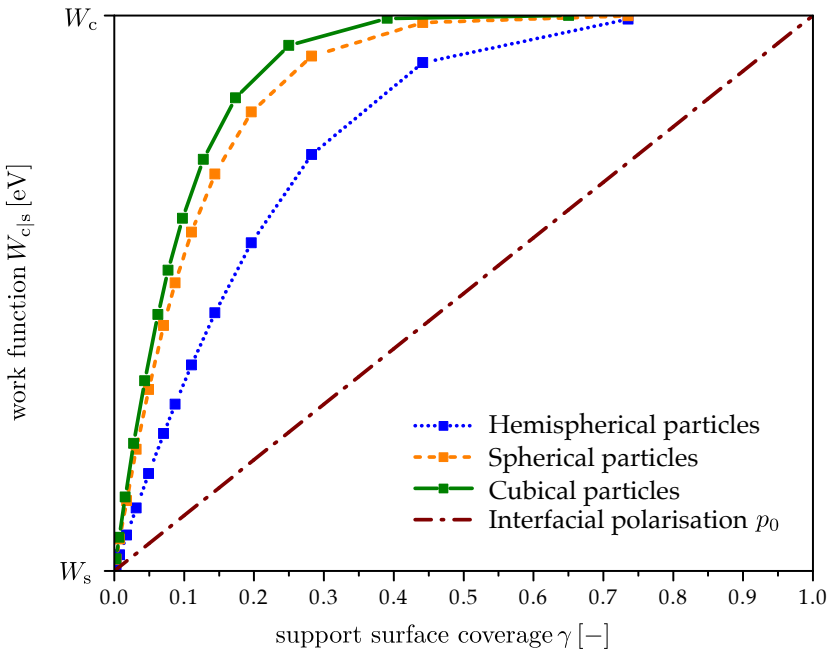

Figure 8. Electrostatic model results. Global work function $W_{c|s}$ as a function of the support surface coverage with catalyst particles $\gamma = A_c/A_{total}$ for different catalyst particle geometries.

electrodes of a capacitor at a voltage equal to the "built-in" potential difference $\Delta\Phi_{s-c}$ between catalyst and support, which is fixed by the corresponding work function difference $W_c - W_s$. Therefore, enhanced CAOS capacitance is expected in the presence of a dielectric such as water (relative dielectric constant ≈ 80[45]), and, in a strongly polarisable dielectric, CAOS charging could, in principle, reach values up to the order of $1\,|e|$/atom. The long-range electron transfer in the presence of a surrounding dielectric could, therefore, become comparable to the short-range electron transfer at the direct CSI, corresponding to a significant valency change of surface atoms with significant consequences for their catalytic properties. However, whereas charging of the CSI affects only catalytic sites that are both in direct contact with the support surface and accessible for the reactants[15,46], long-range capacitive EMSI can affect all sites at the CAOS of the catalyst nanoparticle as a whole. Therefore, EMSI can act on catalytic sites at a significant distance from the support surface at the nanometer scale despite the strong charge screening of metals.

As counterpart to the catalyst particle CAOS, the surrounding empty support surface gets charged at the same magnitude but with opposite sign, cf. Figure 2. Corresponding

modifications of the co-catalytic properties of oxide supports can be expected in accordance with the electron theory of catalysis on semiconductors[47]. It is, therefore, interesting to contemplate EMSI also in a context of catalytic spillover effects[48].

Finally, the long-range charge transfer to the CAOS depends on the degree to which the support material can provide mobile electrons to equilibrate with the catalyst particle. In case of a support material with low density of mobile charge carriers, the formation of a thick depletion layer inside the support decreases the overall capacity of the catalyst CAOS–support system and results in reduced CAOS charging. Thus, capacitive EMSI are strongest for metallic, weaker for semiconducting, and vanishing for insulating support materials. Introducing free charge carriers into a semiconducting or insulating support therefore increases capacitive EMSI with bearings on the catalytic properties of supported catalyst particles. This provides motivation to surface treat or dope supports in heterogeneous catalysis applications with a view to provide free charge carriers even though electronic conductivity of the support is not strictly needed.

For a more detailed quantification of the catalytic effects of capacitive EMSI for specific reactions, DFT calculations of binding energies of probe atoms/molecules at the CAOS of supported metal catalyst particles are necessary. In order to observe strong effects due to capacitive EMSI, such computations of adsorbate binding energies must be carried out for systems with very large supercell in the DFT model corresponding to low coverage of the support surface with catalyst particles. Since the required massive computational resources for this purpose exceeded the ones available within the present study, such detailed quantification for specific reactions remains topic of future research on capacitive EMSI.

IV. CONCLUSIONS

Electronic equilibration between metallic catalyst particles and support material results in long-range charging of the catalytically active outer surface of catalyst particles at the nanometer scale bypassing the strong charge screening of the catalyst particle bulk. In this way, electronic metal–support interactions can affect remote catalytic sites at a significant distance from the direct catalyst–support interface. This long-range charge transfer scales with the work function difference between catalyst and support material, and it depends on the size, shape, and proximity of the catalyst nanoparticles, which suggests a close

connection between such capacitive EMSI and well-established catalyst particle size and proximity effects. Furthermore, strongest catalytic effects are predicted in the presence of a dielectric due to the scaling of CAOS charging with the relative dielectric constant of the surrounding medium.

ACKNOWLEDGMENTS

Financial support from the Swiss Competence Center Energy and Mobility (CCEM) and Umicore AG & Co. KG Germany within the DuraCat project as well as the STFC Global Challenges Network in Batteries and Electrochemical Energy Devices (STFCBatteries.org, grant number ST/K00171X/1) is gratefully acknowledged. This work used the ARCHER UK National Supercomputing Service (http://www.archer.ac.uk), partially via our membership of the UK's HEC Materials Chemistry Consortium, which is funded by EPSRC (EP/L000202), and the IRIDIS High Performance Computing Facility and associated support services at the University of Southampton.

Appendix A: Computational details for DFT

Periodic DFT computations were performed using the *Vienna Ab Initio Simulation Package* (VASP). The core electrons were taken into account by the projector augmented wave method (PAW)[25,26]. The generalized gradient approximation (GGA) in the PBE form[27] was used for the exchange-correlation functional. The simulated system consisted of cuboctahedral Pt_{55} clusters supported on Sb-doped SnO_2 slabs comprising nine atomic layers with the most stable (110) surface orientation of the rutile crystal structure. Both stoichiometric (oxidized) and reduced (110) surfaces of the oxide support were studied. In the latter case, the topmost row of oxygen atoms was removed from the (110) surface. The detailed atomic coordinates for all investigated systems are specified in the POSCAR input files for VASP which are provided as Supplemental Material[49]. The Pt_{55} clusters were placed symmetrically on both support slab surfaces in order to avoid problems with long-range dipole interactions between adjacent images of the catalyst decorated slabs generated by the periodic boundary conditions. The energy cutoff of the plane wave basis set for the wave functions was chosen at $E_{\mathrm{cutoff}} = 500\,\mathrm{eV}$. The extension of the periodic supercells in z-direction perpendicular to the

surface was chosen large enough to accommodate a vacuum region of $\approx 1.6\,\mathrm{nm}$ in between adjacent images. In x- and y-direction, the smaller supercells (1x1) measured $\approx 1.3\,\mathrm{nm}$ containing eight unit cells of the SnO_2 (110) surface. Due to the diameter of the Pt_{55} cluster of $\approx 1.0\,\mathrm{nm}$, the spacing between adjacent Pt_{55} clusters was only $\approx 0.3\,\mathrm{nm}$ resulting in a high support surface coverage $\gamma = A_{\mathrm{Pt}}/A_{\mathrm{total}} \approx 0.6$. The Pt/reduced Sb-$SnO_2$ system was furthermore investigated with a large supercell comprising 2x2 the dimension of the small supercell in x- and y-direction, yielding a coverage $\gamma \approx 0.15$. Only the Γ-point in reciprocal k-space was sampled due to the large size of the system. Computations were performed both on the IRIDIS High Performance Computing Facility, University of Southampton, UK, and on the ARCHER UK National Supercomputing Service.

The lattices of the Pt cluster and of the SnO_2 slabs were fixed for the individual systems and atomic relaxation of the combined system was switched off in the calculations. In this way, structural interactions between catalyst and support were excluded. Only the distance between the Pt cluster and the support (110) surface was relaxed until an energy minimum was reached. The lattice constant of the *fcc* Pt unit cell was determined in a fully-relaxed Pt bulk calculation to $a_{\mathrm{Pt}} = 3.967\,\text{Å}$. A first attempt of a fully-relaxed bulk SnO_2 calculation yielded a band gap of $\approx 0.4\,\mathrm{eV}$, which is much smaller than experimentally observed values $> 3\,\mathrm{eV}$. Therefore, in order to obtain an SnO_2 band gap of $E_{\mathrm{g}} = 2.3\,\mathrm{eV}$, it was decided to fix the lattice constants of the SnO_2 body centered tetragonal unit cell at $a_{SnO_2} = b_{SnO_2} = 4.5\,\text{Å}$ and $c_{SnO_2} = 3.1\,\text{Å}$, which still agrees well with experimentally determined unit cell parameters. The Sb-doped support slabs were constructed by replacing five evenly distributed Sn atoms by Sb atoms (per smaller supercell), corresponding to a support composition of $Sb_{0.035}Sn_{0.965}O_2$.

Work functions were determined as the difference between the plateau value of the electrostatic Hartree potential in the vacuum region and the Fermi level of the system, $W = \Phi_{\mathrm{Hartree}}(\mathrm{vac}) - E_{\mathrm{Fermi}}$. The superposition of the electrostatic Hartree potentials of the free Pt clusters and of the bare Sb-doped SnO_2 slabs was subtracted from the electrostatic Hartree potential of the combined system in order to obtain the net electrostatic Hartree potential $\Phi(\mathbf{r})$ due to equilibration. The same procedure was performed with the corresponding electron density distributions in order to obtain the net electron density change due to equilibration. In addition, for an analysis of the net electron transfer between support and Pt particles, Bader charges[28] of each Pt atom of the free Pt clusters were subtracted

from those of the combined system.

Appendix B: Definition of the global work function of the heterogeneous surface

The definition of an appropriate work function (i.e. the energy needed to extract an electron) of the support surface decorated with catalyst particles requires careful consideration. Charge transfer effects between macroscopically distant parts of a surface are usually excluded from the definition of the work function by specifying the final state of the extracted electron as located "just outside" the respective surface[50]. This distinction is well justified, because the electric fields generated by macroscopic charge transfer effects are several orders of magnitude weaker than the direct surface dipole fields. In the present case, however, charge transfer effects occur at a nanoscopic length scale. The corresponding electric field strengths and surface charges are significant for the catalytic function, so that these effects should be included in the definition of the global work function. Thus, in the present case, "just outside" refers to a distance of the order of $10 - 100\,\mathrm{nm}$ from the surface. This definition is identical to the 'area-averaged work function' used extensively in the surface science literature[7,51]. Consequently, the global work function assumes a specific value for the entire heterogeneous surface that can be measured (e.g., by photoemission spectroscopy[51]) and correlated with global catalytic properties such as overall rate constants in heterogeneous catalysis or exchange current densities in electrocatalysis. This definition, however, must be clearly distinguished from the concept of the 'local work function' that is probed at a sub-nanometer distance from the surface, for instance by photoemission of adsorbed xenon (PAX)[37]. This local work function varies spatially over the heterogeneous surface and contributes to catalytic properties of individual, spatially distinct active sites, for instance at the top or at the perimeter of the catalyst particles.

Appendix C: Proof of the relation $\Delta\Phi = \langle p \rangle / (\epsilon_0 \epsilon_r)$

a. Surface multipole expansion. Without loss of generality, a relative dielectric constant of the surrounding medium of $\epsilon_r = 1$ is assumed in the following. A convenient approach to obtain an analytical expression for the net electrostatic potential step $\Delta\Phi$ across a catalyst particle decorated support material surface is a *surface multipole expansion* of the

electrostatic potential

$$\Phi(\mathbf{r}) = \frac{1}{4\pi\epsilon_0}\int \mathrm{d}\mathbf{r}'\frac{\rho(\mathbf{r}')}{|\mathbf{r}-\mathbf{r}'|} = \frac{1}{4\pi\epsilon_0}\int \mathrm{d}x'\mathrm{d}y'\mathrm{d}z'\frac{\rho(x',y',z')}{[(x'-x)^2+(y'-y)^2+(z'-z)^2]^{1/2}}\ , \quad \text{(C1)}$$

where ρ is the net electrical charge density resulting from the electronic equilibration between catalyst particles and support material. This surface multipole expansion consists in a Taylor expansion of the factor $\frac{1}{[(x'-x)^2+(y'-y)^2+(z'-z)^2]^{1/2}}$ in the coordinate z' perpendicular to the surface only, in contrast to the usual multipole expansion in the entire vector $\mathbf{r}'$. The zeroth order term of the surface multipole expansion reads

$$\Phi^{(0)}(x,y,z) = \frac{1}{4\pi\epsilon_0}\int \mathrm{d}x'\mathrm{d}y'\frac{\sigma(x',y')}{[(x'-x)^2+(y'-y)^2+z^2]^{1/2}}\ , \quad \text{(C2)}$$

with the surface charge density $\sigma(x',y') := \int \mathrm{d}z'\rho(x',y',z')$. The first order term reads

$$\Phi^{(1)}(x,y,z) = \frac{1}{4\pi\epsilon_0}\int \mathrm{d}x'\mathrm{d}y'\frac{z\,p(x',y')}{[(x'-x)^2+(y'-y)^2+z^2]^{3/2}}\ , \quad \text{(C3)}$$

with the surface polarization density $p(x',y') := \int \mathrm{d}z'z'\rho(x',y',z')$. We have the freedom to define the origin of the coordinate system at the x- and y-coordinate of the observation point so that $x = y = 0$ in Equation (C3). Furthermore, we introduce two variable transforms, first from (x',y') to polar coordinates (r',ϕ), and then, after factoring out z in the denominator, we transform r' to $r = r'/z$ to yield

$$\Phi^{(1)}(x,y,z) = \frac{1}{2\epsilon_0}\int_0^\infty \mathrm{d}r\,\frac{r\,\tilde{p}(zr)}{[1+r^2]^{3/2}}\ , \quad \text{(C4)}$$

where $\tilde{p}(r') := \frac{1}{2\pi}\int_0^{2\pi}\mathrm{d}\phi\,p(r',\phi)$.

b. Limiting behavior of surface potential multipoles. The zeroth order term $\Phi^{(0)}(x,y,z)$ of the surface multipole expansion is generated by the surface charge density $\sigma(x',y') := \int \mathrm{d}z'\rho(x',y',z')$. This term is symmetric in the coordinate z perpendicular to the surface and therefore it does not contribute to the overall surface potential step $\Delta\Phi := \lim_{z\to\infty}\Phi(x,y,z) - \lim_{z\to-\infty}\Phi(x,y,z)$.

The first order term $\Phi^{(1)}(x,y,z)$ is generated by the surface polarization density $p(x',y') := \int \mathrm{d}z'z'\rho(x',y',z')$. Under the general assumption that the surface polarization density fulfills the limiting property $\lim_{A\to\infty}\frac{1}{A}\int_A p\,\mathrm{d}A = \langle p\rangle$ with a well-defined area averaged surface

polarization density $\langle p \rangle$, the following limiting behavior of $\Phi^{(1)}$ holds:

$$\lim_{z\to\infty} \Phi^{(1)}(x,y,z) = \frac{\langle p \rangle}{2\epsilon_0} \ . \tag{C5}$$

This can be derived directly from equation (C4) with the use of Lemma 1 presented below. Since the first order surface multipole term is antisymmetric in z, the limiting value for $z \to -\infty$ is given by the negative of this expression.

All terms of order > 1 of the surface multipole expansion do not contribute to the overall potential step and thus the work function: Their respective contribution to Φ gains one effective z-factor in the denominator with each increase of the multipole order, thus, yielding a zero limiting value for $|z| \to \infty$. The overall potential step across the surface, therefore, is entirely determined by the average surface polarization density $\langle p \rangle$ and given by the expression

$$\Delta\Phi := \lim_{z\to\infty} \Phi^{(1)}(x,y,z) - \lim_{z\to-\infty} \Phi^{(1)}(x,y,z) = \frac{\langle p \rangle}{\epsilon_0} \ . \tag{C6}$$

Lemma 1. *Given a function $p : \mathbb{R}^2 \to \mathbb{R}$ on the 2-dimensional plane that fulfills the limit*

$$\lim_{A\to\infty} \frac{1}{A} \int_A p \, \mathrm{d}A = \langle p \rangle \tag{C7}$$

with a well-defined area average $\langle p \rangle$, then the following relation holds

$$\lim_{z\to\infty} \int_0^\infty \mathrm{d}r \, \frac{r \, \tilde{p}(zr)}{[1+r^2]^{3/2}} = \langle p \rangle \ , \tag{C8}$$

where $\tilde{p}(r') := \frac{1}{2\pi} \int_0^{2\pi} p(r', \phi) \, \mathrm{d}\phi$ and p is written in terms of polar coordinates (r', ϕ) on the 2-dimensional plane. The existence of the integral on the left-hand-side is implicitly assumed.

Proof. For any given $\epsilon > 0$ we have to find a z_0 so that $\forall z > z_0$ the following holds:

$$\left| \int_0^\infty \mathrm{d}r \, \frac{r \, \tilde{p}(zr)}{[1+r^2]^{3/2}} - \langle p \rangle \right| < \epsilon \ . \tag{C9}$$

By definition of the integral with upper bound ∞, we know that $\exists R > 0$ so that

$$\left| \int_0^\infty \mathrm{d}r \, \frac{r \, \tilde{p}(zr)}{[1+r^2]^{3/2}} - \int_0^R \mathrm{d}r \, \frac{r \, \tilde{p}(zr)}{[1+r^2]^{3/2}} \right| < \frac{\epsilon}{5} \ . \tag{C10}$$

Also, by definition of the integral with upper bound R, we find an $N \in \mathbb{N}$ so that

$$\left| \int_0^R \mathrm{d}r \, \frac{r\,\tilde{p}(zr)}{[1+r^2]^{3/2}} - \sum_{i=0}^{N-1} \frac{1}{[1+r_i^2]^{3/2}} \int_{r_i}^{r_{i+1}} \mathrm{d}r \, r\,\tilde{p}(zr) \right| < \frac{\epsilon}{5} \,, \tag{C11}$$

where $r_i := i\,\frac{R}{N} = i\,\Delta r$. Then we have

$$\begin{aligned} \sum_{i=0}^{N-1} \frac{1}{[1+r_i^2]^{3/2}} \int_{r_i}^{r_{i+1}} \mathrm{d}r \, r\,\tilde{p}(zr) &= \sum_{i=0}^{N-1} \frac{1}{[1+r_i^2]^{3/2}} \frac{1}{z^2} \int_{zr_i}^{zr_{i+1}} \mathrm{d}r' \, r'\,\tilde{p}(r') \\ &= \sum_{i=0}^{N-1} \frac{1}{[1+r_i^2]^{3/2}} \frac{1}{2\pi z^2} \int_{A_i} p \,\mathrm{d}A \,, \end{aligned} \tag{C12}$$

where the last integral extends over the area of the annuli A_i between the radii zr_i and zr_{i+1}. The respective area of annulus A_i is equal to $A_i = 2\pi z^2 \Delta r^2 (i+\frac{1}{2})$, so that we can write

$$\mathrm{LHS} = \sum_{i=0}^{N-1} \frac{(r_i + \frac{1}{2}\Delta r)}{[1+r_i^2]^{3/2}} \,\Delta r \,\frac{1}{A_i} \int_{A_i} p \,\mathrm{d}A \,. \tag{C13}$$

The minimum area of the annuli is $A_0 = \pi z^2 \Delta r^2 = \pi z^2 \left(\frac{N}{R}\right)^2$. Since N and R are already fixed, we can, according to relation (C7), choose a $z_0 > 0$ large enough so that $\forall z > z_0$ and $\forall i$

$$\left| \frac{1}{A_i} \int_{A_i} p \,\mathrm{d}A - \langle p \rangle \right| < \frac{\epsilon/5}{\sum_{j=0}^{N-1} \frac{(r_j + \frac{1}{2}\Delta r)}{[1+r_j^2]^{3/2}} \,\Delta r} \,. \tag{C14}$$

Finally, N and R can already be chosen large enough in the first place, so that also

$$\left| \sum_{i=0}^{N-1} \frac{(r_i + \frac{1}{2}\Delta r)}{[1+r_i^2]^{3/2}} \,\Delta r - \int_0^R \mathrm{d}r \, \frac{r}{[1+r^2]^{3/2}} \right| < \frac{\epsilon/5}{|\langle p \rangle|} \,, \tag{C15}$$

and

$$\left| \int_0^R \mathrm{d}r \, \frac{r}{[1+r^2]^{3/2}} - \int_0^\infty \mathrm{d}r \, \frac{r}{[1+r^2]^{3/2}} \right| < \frac{\epsilon/5}{|\langle p \rangle|} \,. \tag{C16}$$

The integral on the LHS with upper bound ∞ can be analytically evaluated to yield

$$\int_0^\infty \mathrm{d}r \, \frac{r}{[1+r^2]^{3/2}} = 1 \,. \tag{C17}$$

We then conclude

$$
\begin{aligned}
\left|\int_0^\infty \mathrm{d}r\,\frac{r\,\tilde{p}(zr)}{[1+r^2]^{3/2}} - \langle p\rangle\right| = &\left|\int_0^\infty \mathrm{d}r\,\frac{r\,\tilde{p}(zr)}{[1+r^2]^{3/2}} - \int_0^R \mathrm{d}r\,\frac{r\,\tilde{p}(zr)}{[1+r^2]^{3/2}}\right.\\
&+\int_0^R \mathrm{d}r\,\frac{r\,\tilde{p}(zr)}{[1+r^2]^{3/2}} - \sum_{i=0}^{N-1}\frac{1}{[1+r_i^2]^{3/2}}\int_{r_i}^{r_{i+1}}\mathrm{d}r\,r\,\tilde{p}(zr)\\
&+\sum_{i=0}^{N-1}\frac{(r_i+\frac{1}{2}\Delta r)}{[1+r_i^2]^{3/2}}\,\Delta r\,\left(\frac{1}{A_i}\int_{A_i} p\,\mathrm{d}A - \langle p\rangle\right)\\
&+\langle p\rangle\left(\sum_{i=0}^{N-1}\frac{(r_i+\frac{1}{2}\Delta r)}{[1+r_i^2]^{3/2}}\,\Delta r - \int_0^R \mathrm{d}r\,\frac{r}{[1+r^2]^{3/2}}\right)\\
&\left.+\langle p\rangle\left(\int_0^R \mathrm{d}r\,\frac{r}{[1+r^2]^{3/2}} - \int_0^\infty \mathrm{d}r\,\frac{r}{[1+r^2]^{3/2}}\right)\right|\\
\le &\left|\int_0^\infty \mathrm{d}r\,\frac{r\,\tilde{p}(zr)}{[1+r^2]^{3/2}} - \int_0^R \mathrm{d}r\,\frac{r\,\tilde{p}(zr)}{[1+r^2]^{3/2}}\right|\\
&+\left|\int_0^R \mathrm{d}r\,\frac{r\,\tilde{p}(zr)}{[1+r^2]^{3/2}} - \sum_{i=0}^{N-1}\frac{1}{[1+r_i^2]^{3/2}}\int_{r_i}^{r_{i+1}}\mathrm{d}r\,r\,\tilde{p}(zr)\right|\\
&+\sum_{i=0}^{N-1}\frac{(r_i+\frac{1}{2}\Delta r)}{[1+r_i^2]^{3/2}}\,\Delta r\,\left|\frac{1}{A_i}\int_{A_i} p\,\mathrm{d}A - \langle p\rangle\right|\\
&+|\langle p\rangle|\left|\sum_{i=0}^{N-1}\frac{(r_i+\frac{1}{2}\Delta r)}{[1+r_i^2]^{3/2}}\,\Delta r - \int_0^R \mathrm{d}r\,\frac{r}{[1+r^2]^{3/2}}\right|\\
&+|\langle p\rangle|\left|\int_0^R \mathrm{d}r\,\frac{r}{[1+r^2]^{3/2}} - \int_0^\infty \mathrm{d}r\,\frac{r}{[1+r^2]^{3/2}}\right|\\
<&\frac{\epsilon}{5}+\frac{\epsilon}{5}+\frac{\epsilon}{5}+\frac{\epsilon}{5}+\frac{\epsilon}{5} = \epsilon\ . \qquad \text{(C18)}
\end{aligned}
$$

□

---

* tobias.binninger@psi.ch

† d.kramer@soton.ac.uk

[1] G. Ertl and H.-J. Freund, Phys. Today **52**, 32 (1999).

[2] G. Ertl, H. Knözinger, F. Schüth, and J. Weitkamp, eds., *Handbook of Heterogeneous Catalysis*, 2nd ed. (Wiley, 2008).

[3] G.-M. Schwab, J. Block, and D. Schultze, Angew. Chem. **71**, 101 (1959).

[4] R. P. Eischens, in *The Surface Chemistry of Metals and Semiconductors*, edited by H. C. Gatos (John Wiley & Sons, Inc., 1959) pp. 421–438.

[5] A. Y. Stakheev and L. M. Kustov, Appl. Catal., A **188**, 3 (1999).

[6] C. T. Campbell, Nature Chem. **4**, 597 (2012).

[7] C. T. Campbell, Surf. Sci. Rep. **27**, 1 (1997).

[8] A. Sanchez, S. Abbet, U. Heiz, W.-D. Schneider, H. Häkkinen, R. N. Barnett, and U. Landman, J. Phys. Chem. A **103**, 9573 (1999).

[9] W. Wei, Y. Dai, M. Guo, and B. Huang, Appl. Surf. Sci. **257**, 6607 (2011).

[10] A. Bruix, J. A. Rodriguez, P. J. Ramírez, S. D. Senanayake, J. Evans, J. B. Park, D. Stacchiola, P. Liu, J. Hrbek, and F. Illas, J. Am. Chem. Soc. **134**, 8968 (2012).

[11] G. Pacchioni, Phys. Chem. Chem. Phys. **15**, 1737 (2013).

[12] X. Lin, N. Nilius, H.-J. Freund, M. Walter, P. Frondelius, K. Honkala, and H. Häkkinen, Phys. Rev. Lett. **102**, 206801 (2009).

[13] L. Li, A. H. Larsen, N. A. Romero, V. A. Morozov, C. Glinsvad, F. Abild-Pedersen, J. Greeley, K. W. Jacobsen, and J. K. Nørskov, J. Phys. Chem. Lett. **4**, 222 (2013).

[14] F. Solymosi, Catal. Rev. **1**, 233 (1968).

[15] T. Ioannides and X. E. Verykios, J. Catal. **161**, 560 (1996).

[16] Y. Lykhach, S. M. Kozlov, T. Skala, A. Tovt, V. Stetsovych, N. Tsud, F. Dvorak, V. Johanek, A. Neitzel, J. Myslivecek, S. Fabris, V. Matolin, K. M. Neyman, and J. Libuda, Nat. Mater. **15**, 284 (2016).

[17] N. D. Lang and W. Kohn, Phys. Rev. B **7**, 3541 (1973).

[18] R. W. Joyner, J. B. Pendry, D. K. Saldin, and S. R. Tennison, Surf. Sci. **138**, 84 (1984).

[19] V. Tripković, F. Abild-Pedersen, F. Studt, I. Cerri, T. Nagami, T. Bligaard, and J. Rossmeisl, ChemCatChem **4**, 228 (2012).

[20] Y.-G. Wang, Y. Yoon, V.-A. Glezakou, J. Li, and R. Rousseau, J. Am. Chem. Soc. **135**, 10673 (2013).

[21] V. P. Zhdanov, Surf. Sci. **512**, L331 (2002).

[22] T. Ioannides, Surf. Sci. **530**, 216 (2003).

[23] F. Takasaki, S. Matsuie, Y. Takabatake, Z. Noda, A. Hayashi, Y. Shiratori, K. Ito, and K. Sasaki, J. Electrochem. Soc. **158**, B1270 (2011).

[24] T. Binninger, R. Mohamed, A. Patru, K. Waltar, E. Gericke, X. Tuaev, E. Fabbri, P. Levecque, A. Hoell, and T. J. Schmidt, Chem. Mater. **29**, 2831 (2017).

[25] P. E. Blöchl, Phys. Rev. B **50**, 17953 (1994).

[26] G. Kresse and D. Joubert, Phys. Rev. B **59**, 1758 (1999).

[27] J. P. Perdew, K. Burke, and M. Ernzerhof, Phys. Rev. Lett. **77**, 3865 (1996).

[28] W. Tang, E. Sanville, and G. Henkelman, J. Phys.: Condens. Matter **21**, 084204 (2009).

[29] V. T. T. Ho, C. J. Pan, J. Rick, W. N. Su, and B. J. Hwang, J. Am. Chem. Soc. **133**, 11716 (2011).

[30] F. Behafarid, L. K. Ono, S. Mostafa, J. R. Croy, G. Shafai, S. Hong, T. S. Rahman, S. R. Bare, and B. R. Cuenya, Phys. Chem. Chem. Phys. **14**, 11766 (2012).

[31] R. F. Baddour and M. C. Deibert, J. Phys. Chem. **70**, 2173 (1966).

[32] M. Nesselberger, M. Roefzaad, R. F. Hamou, P. U. Biedermann, F. F. Schweinberger, S. Kunz, K. Schloegl, G. K. H. Wiberg, S. Ashton, U. Heiz, K. J. J. Mayrhofer, and M. Arenz, Nat. Mater. **12**, 919 (2013).

[33] M. Che, Catal. Today **218-219**, 162 (2013).

[34] A. J. Medford, A. Vojvodic, J. S. Hummelshøj, J. Voss, F. Abild-Pedersen, F. Studt, T. Bligaard, A. Nilsson, and J. K. Nørskov, J. Catal. **328**, 36 (2015).

[35] J. Greeley, I. E. L. Stephens, A. S. Bondarenko, T. P. Johansson, H. A. Hansen, T. F. Jaramillo, J. Rossmeisl, I. Chorkendorff, and J. K. Nørskov, Nature Chem. **1**, 552 (2009).

[36] P. Liu, A. Logadottir, and J. K. Nørskov, Electrochim. Acta **48**, 3731 (2003).

[37] K. Wandelt, Appl. Surf. Sci. **111**, 1 (1997).

[38] J. H. Block, in *Actes du Deuxième Congrès International de Catalyse, Paris, 1960* (Editions Technip, Paris, 1961) p. 1644.

[39] Z.-P. Liu, X.-Q. Gong, J. Kohanoff, C. Sanchez, and P. Hu, Phys. Rev. Lett. **91**, 266102 (2003).

[40] B. Hammer and J. K. Nørskov, Nature **376**, 238 (1995).

[41] M. Mavrikakis, B. Hammer, and J. K. Nørskov, Phys. Rev. Lett. **81**, 2819 (1998).

[42] B. Hammer and J. K. Nørskov, in *Impact of Surface Science on Catalysis*, Advances in Catalysis, Vol. 45, edited by B. Gates and H. Knoezinger (Academic Press, 2000) pp. 71–129.

[43] W. M. Haynes, D. R. Lide, and T. J. Bruno, eds., *CRC Handbook of Chemistry and Physics*, 96th ed. (CRC Press, 2015) pp. 12–122.

[44] J. K. Nørskov, J. Rossmeisl, A. Logadottir, L. Lindqvist, J. R. Kitchin, T. Bligaard, and

H. Jónsson, J. Phys. Chem. B **108**, 17886 (2004).

[45] W. M. Haynes, ed., *CRC Handbook of Chemistry and Physics*, 97th ed. (CRC Press/Taylor & Francis, Boca Raton, FL, Internet Version 2017).

[46] X. Lin, B. Yang, H.-M. Benia, P. Myrach, M. Yulikov, A. Aumer, M. A. Brown, M. Sterrer, O. Bondarchuk, E. Kieseritzky, J. Rocker, T. Risse, H.-J. Gao, N. Nilius, and H.-J. Freund, J. Am. Chem. Soc. **132**, 7745 (2010).

[47] T. Wolkenstein (Academic Press, 1960) pp. 189–264.

[48] R. Prins, Chem. Rev. **112**, 2714 (2012).

[49] See Supplemental Material at [URL] for POSCAR input files for VASP DFT calculations which contain the atomic coordinates of the models. POSCAR files are given for the small supercell (1x1) systems with stoichiometric and reduced support surface, and for the large supercell (2x2) system with reduced support surface.

[50] N. W. Ashcroft and N. D. Mermin, *Solid State Physics* (Harcourt College Publishers, 1976) pp. 354–360.

[51] K. H. Ernst, A. Ludviksson, R. Zhang, J. Yoshihara, and C. T. Campbell, Phys. Rev. B **47**, 13782 (1993).